One Pot Synthesis of Ammonium Rich Nickel Hexacyanoferrate as Stable Cathode Material for Ammonium-Ion Batteries

Peng Zhang,[a] Xiangguang Zhang,[a] Dahui Liu,[a] Ao Xiang,[a] Jun Lu,[a] Yan Jiang,[a] Ze Yang,*[b] and Pei Hu*[a]

Rechargeable aqueous batteries based on ammonium-ion (NH_4^+) redox reactions shows great potential for large-scale energy-storage due to its plentiful supplies, environmental friendliness, intrinsic security, and sustainability. Prussian blue analogues (PBAs) are regarded to be one of the most promising electrode materials owning to high energy storage density, ease of synthesis, and excellent electrochemical performances. However, the synthesis of ammonium rich Prussian blue analogues is too complicated. Herein, a one pot synthesis of NH_4^+-rich nickel hexacyanoferrate (NNiHCF) is developed and the NH_4^+ storage chemistry is investigated. NNiHCF cathode is coupled with an activated carbon (AC) anode and $(NH_4)_2SO_4$ aqueous electrolyte to assemble ammonium-ion batteries. The aqueous full cell demonstrates good electrochemical performance, such as $50.2\ mAh\,g^{-1}$ at the current rate of 2 C, and 60% capacity retention in 5000 cycles. Furthermore, the fundamental characteristics of the reversible redox reaction and the durable structure of NNiHCF are revealed by X-ray diffraction (XRD) and electrochemical measurements. This work proposes a facile method for the synthesis of ammonium-rich Prussian.

Introduction

Li-ion batteries, characterized by high efficiency, portability, and high energy storage density, can serve as an effective energy storage solution for solar and wind energy.[1] However, organic electrolytes in Li-ion batteries suffer from their inherent volatility, poor thermal stability, high cost, maintenance requirements and even toxicity.[2] Consequently, there is an urgent need to find an alternative energy storage system that can replace organic batteries. Aqueous batteries have become one of the promising candidates for large-scale energy storage due to high safety, environmental friendliness, low cost, lightweight and wide application prospects which surpass organic electrolyte systems.[3]

Compared to aqueous metal ion batteries (Li^+, Na^+, K^+ and Zn^{2+}), non-metal ammonium ions possess unique advantages, such as low molar mass, relatively small hydrated ion size, and unique hydrogen bond coordination structure.[4] Most importantly, NH_4^+ are abundant resources that can be artificially synthesized from readily available nitrogen and hydrogen

elements on Earth, making them theoretically limitless and renewable.[5] Therefore, ammonium ion batteries (AIB) may present a more promising potential for energy storage applications.

Significant research progress has been made in the development of energy storage devices for aqueous AIB. A series of electrode materials suitable for NH_4^+ storage has been developed. To date, the materials storing ammonia mostly used for AIB mainly include Prussian blue analogues,[6] layered oxides, Ti_3C_2 MXenes,[7] $NH_4V_4O_{10}$,[8] MnO_x,[9] V_2O_5,[10] MoO_3,[11] WO_3[12] and covalent organic frameworks (COFs).[13] Recently, Prussian blue analogues (PBAs) are regarded as one of the most prospective electrode materials owning to high energy storage density, ease of synthesis, and excellent electrochemical performances.[6a,14] Prussian blue (PB) consists of a three-dimensional framework that provides sufficient space for efficient ion storage and transfer, resulting in a higher energy storage density.[15] Moreover, $A_xL_y[M(CN)_6]_z\cdot nH_2O$ is the typical formula for PBAs, where A stands for monovalent ions (also known as alkali metal ions, ammonium ions or other metal ions), while L and M stand for transition metal ions. Through octahedral coordination, the transition metal ions coordinate with six nitrogen atoms and one carbon atom to form the framework of PBAs.[6a,16] During discharge, monovalent ions can be released from the skeleton of PBAs. PBAs can undergo repeated charge-discharge cycles without significant degradation in electrochemical performance, which is a crucial characteristic for their application as electrode materials.[6b,17] The development of high-performance ammonium-rich PB cathode materials is of great significance and challenge, benefiting from the abundant ammonium resources on Earth. Previously, the synthesis of ammonium-rich PB materials usually involved two-step methods (e.g., co-precipitation and ion exchange), which unavoid-

[a] Dr. P. Zhang, X. Zhang, D. Liu, A. Xiang, J. Lu, Dr. Y. Jiang, Dr. P. Hu
School of Science,
Hubei University of Technology
Wuhan, 430068, China
E-mail: hupei@hbut.edu.cn

[b] Dr. Z. Yang
Institute of Nanoscience and Nanotechnology, College of Physical Science and Technology
Central China Normal University
Wuhan, Hubei 430079, China
E-mail: yz@ccnu.edu.cn

Batteries & Supercaps

Research Article
doi.org/10.1002/batt.202300546

Chemistry
Europe
European Chemical
Societies Publishing

ably resulted in long synthesis cycles, high cost and low productivity.[6b,18]

Herein, a one-pot strategy for the synthesis of ammonium-rich PB material through a simple co-precipitation method are demonstrated for the first time. NNiHCF was used as the cathode, AC as the anode, and $(NH_4)_2SO_4$ solution as the electrolyte to assemble a full cell. The full cell exhibits superior cyclic performance and capacity retention, achieving a specific capacity of 50.2 mAh g^{-1} at a current density of 2 C. After 5000 cycles, the capacity retention was 60%. Furthermore, the structural changes and electrochemical states of NNiHCF upon NH_4^+ insertion/deinsertion were analyzed using non-in situ XRD analysis. These results revealed that NNiHCF synthesized directly through co-precipitation is a highly reversible and structurally stable cathode material. Here, we present a method for synthesizing ammonium-rich PB using co-precipitation. The exceptional long-term cycling performance and capacity retention suggest that PBAs holds promise as a future cathode material.

Results and Discussion

NNiHCF powder was fabricated by a one-pot co-precipitation method at room temperature using $Na_4[Fe(CN)_6]$, $NiSO_4$, and $(NH_4)_2SO_4$ as starting precursors. The fresh NNiHCF powder exhibits a yellow-green color, as shown in Figure S1. Powder XRD was performed to demonstrate the crystal structure of NNiHCF. NNiHCF shows a typical face-centered cubic structure with Fm-3 m space group, as depicted in Figure 1a. The characteristic crystal planes (200), (220), (400), (420), (422), (440), (600), and (620) could be easily observed in the XRD pattern,

indicating the attainment of pure NNiHCF and the absence of impurity phases. Figure 1b shows iron and nickel ions are interconnected through cyanide groups in the crystal structure of NNiHCF, forming a 3D Fe—CN—Ni skeleton with ammonium ions accommodated at the 8c site.[6b] SEM images revealed that NNiHCF displays uniform nanoparticles which is shown in inset of Figure S2. Figure S2 shows particle size distribution of NNiHCF powder. The particle size of NNiHCF powder mainly distributes in the range of 0.4~200 nm.

Figure 1c shows FT-IR of NNiHCF powder. It exhibits two peaks at 3230 and 1415 cm^{-1} which can be ascribed to the stretching vibration and in-plane vibration of the N—H bonds in ammonia ions, respectively.[5a] A strong and sharp adsorption peak was detected at 2095 cm^{-1}, which can be assigned to the stretching vibration of —C≡N- in the Fe^{2+}—CN—Ni^{2+} moieties.[6b] The FT-IR spectrum indicates the presence of a trace quantity of H_2O in NNiHCF. To confirm the chemical composition of NNiHCF, several complementary techniques were employed. Thermal gravimetric analysis (TGA) was performed under a nitrogen atmosphere from room temperature to 700 °C to determine the water content, and the TGA curve is shown in Figure 1d. Below 200 °C, a noticeable initial weight loss of approximately 17.3% is observed, which can be explained by the detachment of crystalline and adsorbed water molecules. (Table S1). The formula of NNiHCF are determined to be $(NH_4)_{1.50}Ni[Fe(CN)_6]_{0.83}\cdot\square_{0.17}\cdot2.9H_2O$. The non-stoichiometry of Fe to Ni indicates the missing of some $[Fe(CN)_6]^{4-}$ as defects in the lattice, which is expressed as $\square$ in the formula.

Furthermore, XPS was performed to determine the oxidation states of elements on the surface of NNiHCF. The Fe 2p region exhibits two peaks at 708.6 and 721.48 eV, corresponding to the Fe 2p$_{3/2}$ and Fe 2p$_{1/2}$ spin-orbit orbitals of Fe^{2+}, as
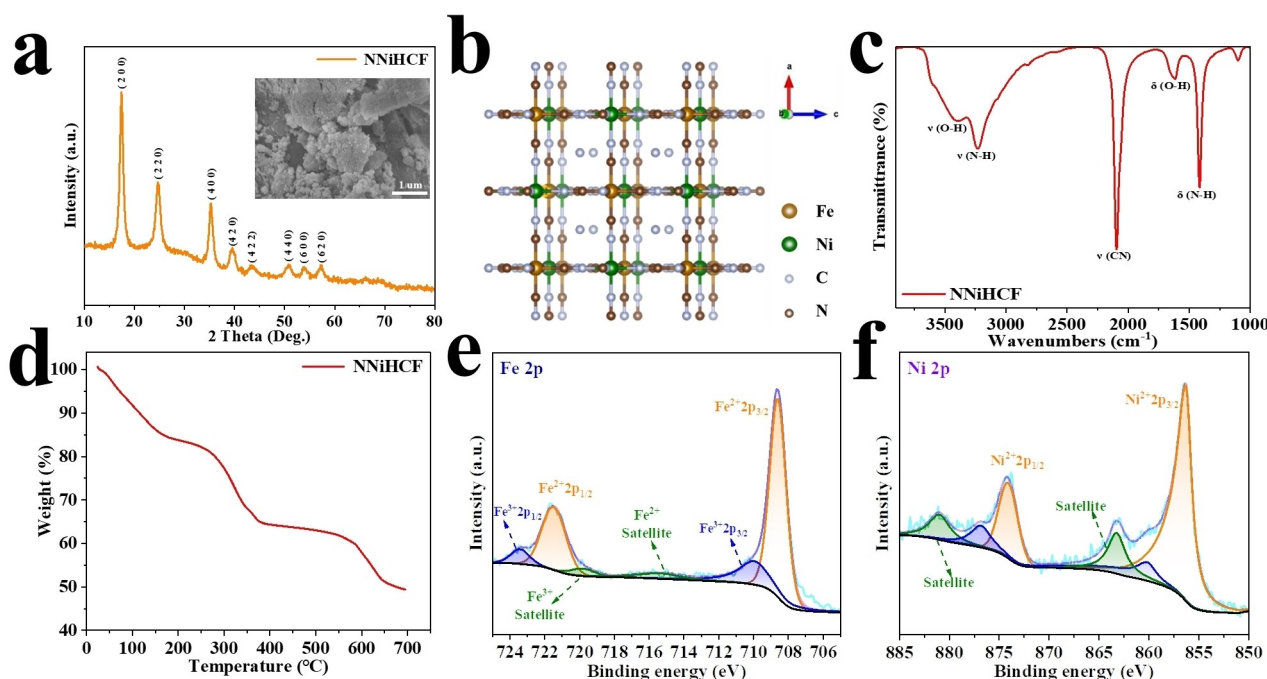

Figure 1. a) XRD pattern for NNiHCF powder. b) A typical unit cell for crystal structure, c) FTIR image, d) TG curve of NNiHCF powder. XPS of e) Fe 2p and f) Ni 2p region.

Batteries & Supercaps

Research Article
doi.org/10.1002/batt.202300546

Chemistry Europe
European Chemical
Societies Publishing

shown in Figure 1e. Additionally, two peaks are detected at 709.96 and 723.41 eV, suggesting the Fe $2p_{3/2}$ and Fe $2p_{1/2}$ spin-orbit orbitals of Fe^{3+}. The existence of Fe^{2+} and Fe^{3+} are also evidenced by the satellite peaks at 715.21 and 719.81 eV, respectively.[19] Figure 1f shows XPS spectrum of the Ni 2p region. Two main peaks can be observed at 856.46 and 874.10 eV, corresponding to the Ni $2p_{3/2}$ and Ni $2p_{1/2}$ spin-orbit orbitals of Ni^{2+}. Satellite features of Ni^{2+} also are detected at 863.05 and 880.96 eV. Thus, the XPS results confirms the coexistence of Ni^{2+}, Fe^{2+}, and Fe^{3+} in NNiHCF.[20]

The electrochemical performances of NNiHCF cathode were systematically evaluated in a three-electrode cell using cyclic voltammetry (CV) and galvanostatic charge/discharge (GCD) tests. NNiHCF served as the working electrode, a carbon rod as the counter electrode, and a saturated calomel electrode (SCE, E = 0.244 V vs. standard hydrogen electrode, SHE) as the reference electrode. Figure 2a presents the first four CV curves of NNiHCF cathode in 2 M $(NH_4)_2SO_4$ and 0.1 M $NiSO_4$ hybrid aqueous electrolyte. The rationale behind the choice of $NiSO_4$ solution as an electrolyte additive will be discussed later. Except for the first cycle, these curves overlap well, demonstrating high reversibility of ammonium ion intercalation/deintercalation. The

CV curves exhibit a broad cathodic current distribution, with peak potentials at 0.644 V (vs. saturated calomel electrode) and two anodic peak potentials at 0.656 and 0.746 V. Previous studies have reported that Ni^{2+} is electrochemically inert in $A_2Ni[Fe(CN)_6]$ (A=Li, Na, and K).[21] The observed redox reactions in this case can be attributed to the $[Fe(CN)_6]^{3-}/[Fe(CN)_6]^{4-}$ couple in NNiHCF electrode with intercalation/deintercalation of NH_4^+ ions. The two oxidation peaks can be attributed to the deintercalation of ions from the defect sites of $[Fe(CN)_6]^{4-}$ and the interior of the intact structure at 8c sites, respectively.[6b]

PBAs usually suffer from a severe metal-ion dissolution during cycling, thereby the relationship between metal-ion dissolution and capacity retention of NNiHCF was investigated to understand capacity fading mechanism of NNiHCF. Consequently, the contents of dissolved Fe ions were compared in the electrolytes with or without $NiSO_4$ additive after cycles. There are 5.3 and 4.4 mg L^{-1} of dissolved Fe ions in 2 M $(NH_4)_2SO_4$ or 2 M $(NH_4)_2SO_4$ and 0.1 M $NiSO_4$ hybrid electrolytes after 50 cycles which is shown in Table S1. Higher dissolution of Fe ions in the cycled $(NH_4)_2SO_4$ electrolytes can explain the capacity fade of NNiHCF cathode without $NiSO_4$ additive. To investigate the effects of $NiSO_4$ addition in the electrolyte, CV
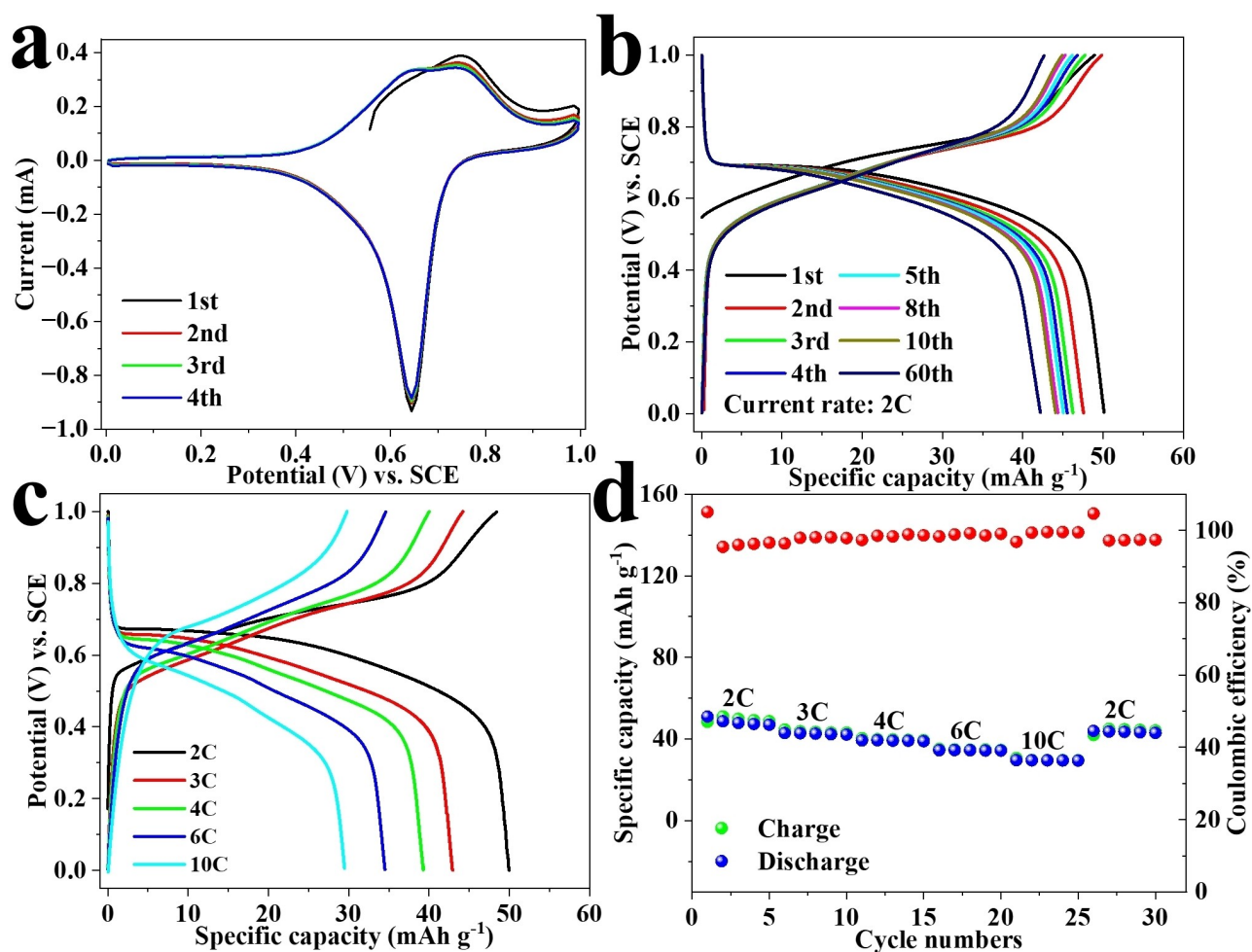
Figure 2. Electrochemical performances of NNiHCF in a three-electrode cell. a) Typical CV curves tested at a scan rate of 0.5 mV s^{-1}. b) The four five GCD curves at 2 C in a range between 0.5 and 1.0 V. c) The GCD curves at 2, 3, 4, 6, and 10 C. d) Rate performance.

Batteries & Supercaps

Research Article
doi.org/10.1002/batt.202300546

**Chemistry
Europe**
European Chemical
Societies Publishing

curves using 0.1 M $NiSO_4$ or 2.0 M $(NH_4)_2SO_4$ as electrolytes are compared in Figure S3. When 0.1 M $NiSO_4$ is used as electrolyte, distinct oxidation and reduction peaks can be distinguished in the CV curve. The oxidation peak at 0.69 V originate from NH_4^+-ion extraction from the framework, which is in accordance with the NH_4^+-ion extraction data in $(NH_4)_2SO_4/NiSO_4$ hybrid electrolyte in Figure 2a. In the subsequent cycles, the redox pair peaks at 0.29/0.48 V can be attributed to Ni^{2+}-ion deintercalate/intercalate from/into the host which is totally different with the feature of NH_4^+-ion deintercalation/intercalation. Figure S4 demonstrates that clear oxidation peaks at 0.624/0.75 V and a reduction peak at 0.626 V are observed when pure 2.0 M $(NH_4)_2SO_4$ is used as electrolyte. These results suggest Ni^{2+}-ion deintercalation/intercalation occurs at lower potential compared to NH_4^+-ion deintercalation/intercalation. It is essentially consistent with potential of NNiHCF cathode cycled in hybrid electrolyte, indicating that Ni^{2+} in the electrolyte does not affect the intercalation of NH_4^+.

Figure 2b illustrates the galvanostatic charge/discharge (GCD) curves of NNiHCF cathode at 2 C (1 C $\approx$ 100 mA g^{-1}) from 0 to 1.0 V vs. SCE. Distinct voltage plateaus of the GCD curves during the initial charge and discharge processes can be observed, indicating the reversible extraction/insertion of NH_4^+ from/into the NNiHCF lattice, which is highly consistent with the CV results. Furthermore, the voltage plateau remains at the similar positions in the subsequent cycles. Additionally, during the initial cycling period, the discharge capacity of NNiHCF cathode is 51.1 mAh g^{-1}. In the subsequent cycles, the capacity slightly fades with a CE of approximately 100%. Figures 2c and 2d present discharge capacity of 50.9, 42.9, 39.2, 34.5, and 29.4 mAh g^{-1} at 2, 3, 4, 6, and 10 C, respectively. Besides the CV experiments, GCD was employed to investigate the contribution of Ni^{2+} to the capacity. Figure S5 shows the corresponding GCD curves of NNiHCF cathode where 0.1 M $NiSO_4$ solution was used as electrolyte. It is evident that intercalation of Ni^{2+} ions displays a plateau at about 0.4 V during cycling which is in accordance with the CV results. Furthermore, the first five GCD curves with pure 2.0 M $(NH_4)_2SO_4$ as electrolyte are shown in Figure S6. It is apparent that the shape and capacity of the GCD curves highly match those cycled in the hybrid electrolyte. It indicates the overall capacity of NNiHCF cycled in the hybrid electrolyte is provided by ammonium ions insertion/extraction. Additionally, it can be verified that the form and voltage plateau location of the charge and discharge curves during the NH_4^+ insertion/extraction process are not significantly affected by the presence of Ni^{2+}, as seen by the identical shapes of the GCD curves in the pure $(NH_4)_2SO_4$ and hybrid electrolyte. Therefore, the attained capacity of Ni^{2+} can be neglected and the presence of Ni^{2+} in the electrolyte has little influence on the electrochemical reactions during NH_4^+ insertion/extraction.

To investigate the capacitance and diffusion contribution of NNiHCF cathode, CV curves at various scan rates from 0.1 to 2.0 mV s^{-1} were collected and shown in Figure 3a and Figure S7. As the scan rate increases, the initial shape of the CV curves remains almost unchanged, indicating the fast response of NNiHCF cathode at high scan rates.[22] Generally, the peak current (i) measured from the CV curves and the corresponding
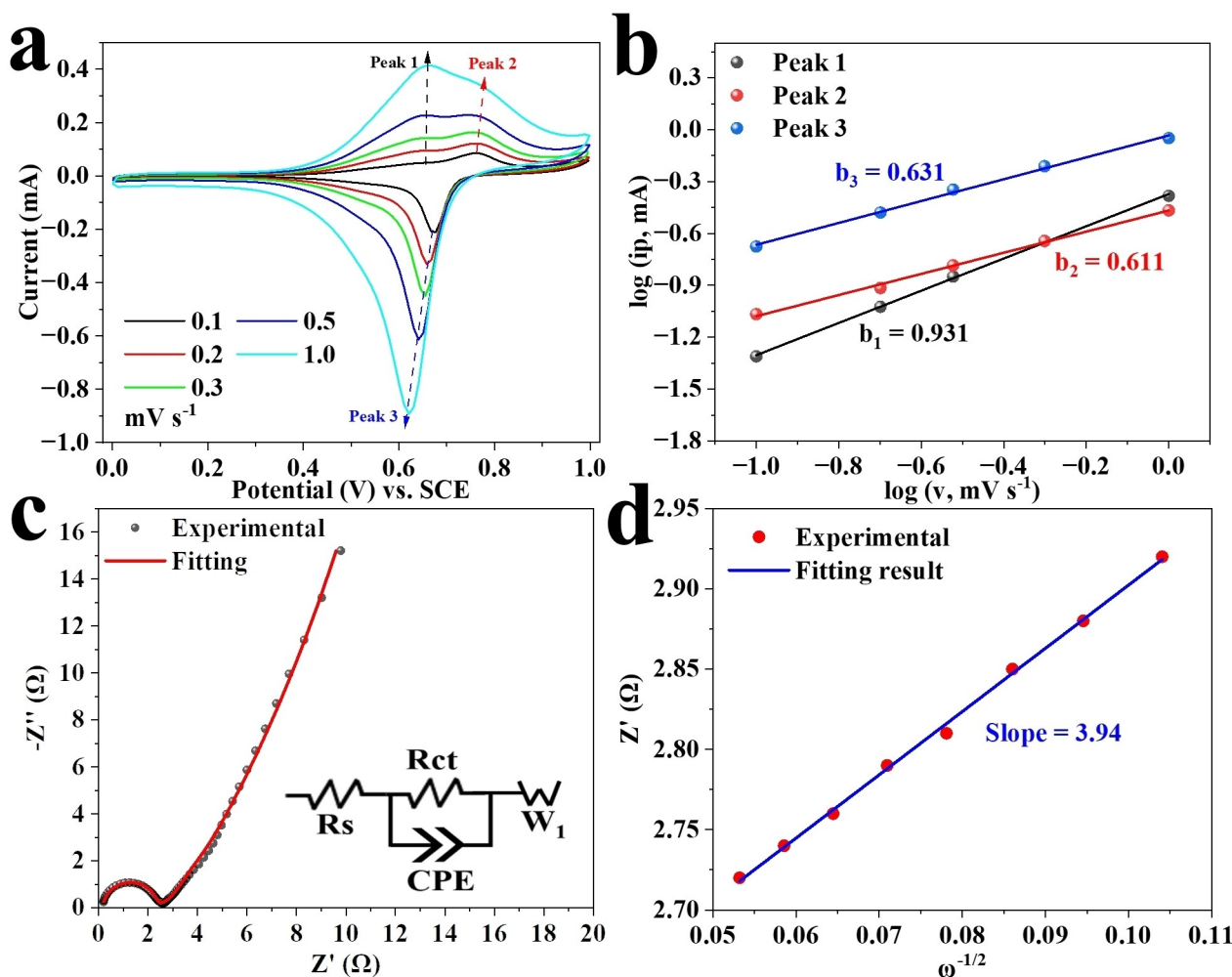
scan rate (v) can be expressed as follows: $i = av^b$. This expression can be written as $\log(i) = b\ \log(v) + \log(a)$, where i, v, and a represent the current density, scan rate, and fitting parameter, respectively.[13,23] The slope of $\log(v)$ and $\log(i)$ is commonly used to determine the exponential factor (b), which directly evaluates the electrochemical diffusion behavior of NH_4^+ storage. When b value approaches 0.5, it suggests semi-infinite diffusion-limited behavior, while b value close to 1 idicates capacitive behavior dominated by fast interface reactions.[24] The calculated b values from Figure 3b are 0.631, 0.611 and 0.931, respectively, suggesting that peak 1 is dominate by capacitive behavior while peak 2 and 3 refer to more diffusion characteristics.

In order to investigate the electrochemical kinetics of NNiHCF electrode, EIS measurements were conducted to analyze the charge transfer processes and diffusion limitations. Figures 3c present the experimental and fitted EIS curves of the NNiHCF electrode, respectively. The values of the equivalent series resistance (R_s) and charge transfer resistance (R_{ct}) are determined to be 0.143 and 2.357 Ω, respectively. The relationship between the real part (Z') and angular frequency (ω) can be described by the following equation: $Z' = R_s + R_{ct} + \sigma\omega^{-1/2}$, where σ represents the Warburg coefficient.[25] Figure 3d demonstrates the slope of the fitted line Z' - $\omega^{-1/2}$, which yields a Warburg coefficient of 3.94 for NNiHCF cathode. According to previously literature, the ion diffusion coefficient is inversely proportional to the slope of the fitted line Z' - $\omega^{-1/2}$.[26] Thus, the Warburg coefficient indicates an excellent charge diffusion capability.

To reveal the structural evolution of NNiHCF during NH_4^+ intercalation/deintercalation processes, XRD patterns were recorded at various state of charge (SOC). Figure 4a and 4b present typical charge-discharge curves of NNiHCF cathode and corresponding XRD patterns at various state of charge, respectively. All XRD patterns remains similar without new peak formation, indicating that NNiHCF maintains its cubic structure during NH_4^+ intercalation/deintercalation, referring to a quasi-solid solution reaction. Figure 4c shows the magnified diffraction peaks of various crystal planes. It can be observed that all diffraction peaks shift to lower angles during charging and returned to their original positions during discharging, indicating lattice expansion during NH_4^+ deintercalation and lattice contraction during NH_4^+ intercalation into NNiHCF.[6b,15a] Similar phenomena have been reported in PBAs, where the lattice contraction is attributed to the shortening of Fe—C bond distances during NH_4^+ intercalation into NNiHCF framework during discharge.[27] Furthermore, the slight angular deviation demonstrates nearly zero strain during NH_4^+ insertion/extraction processes in NNiHCF which is in accordance with the previously reported intercalation of NH_4^+. In theory, the redox peaks should emerge with the insertion/extraction of cations in cubic NNiHCF, which are assigned to the valence changes of $Fe^{2+}/Fe^{3+}\equiv C$ couple.[25] In summary, the excellent cycling performances of NNiHCF during charge-discharge contributes to its highly reversible structural evolution.

A rocking-chair type full cell was assembled using NNiHCF as the cathode and AC as the anode in a hybrid electrolyte

Batteries & Supercaps

Research Article
doi.org/10.1002/batt.202300546

Chemistry
Europe
European Chemical
Societies Publishing

Figure 3. a) CV curves tested at various scan rates. b) The relationship between logarithm cathodic peak current and logarithm scan rates. c) Nyquist and fitting plots (inset is equivalent electric circuit). d) The relationship between Z′ and $\omega^{-1/2}$ at low frequency.
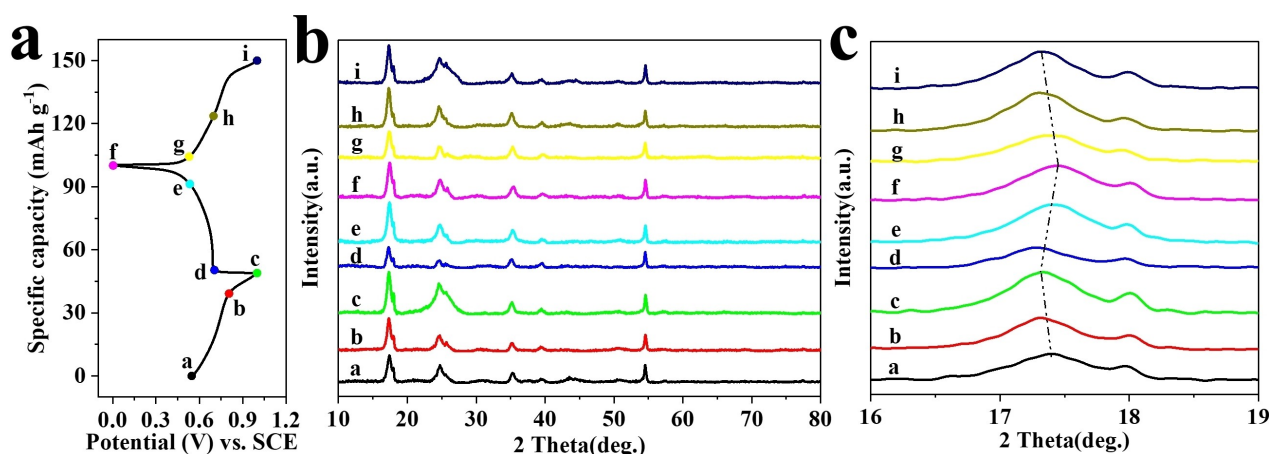
Figure 4. a) Typical charge/discharge curves of the NNiHCF cathode. b) and c). Corresponding ex situ XRD patterns at various SOC, as marked in c.

containing 2.0 M $(NH_4)_2SO_4$ and 0.1 M $NiSO_4$. During charge, NNiHCF cathode undergoes NH_4^+ deintercalation reaction, while AC anode undergoes ammonium ion adsorption. The reverse process occurs during discharge. As shown in Figure S8,

the capacity of the full cell using 2.0 M $(NH_4)_2SO_4$ electrolyte decreases from 49.5 to 20.3 mAh g^{-1} after 3500 cycles with a capacity retention of only 40.3 %. These results confirm that the dissolution of metal ions can inhibit the attenuation of capacity.

Batteries & Supercaps

Research Article
doi.org/10.1002/batt.202300546

**Chemistry Europe**
European Chemical
Societies Publishing

Additionally, the electrochemical performances of the NNiHCF cathode cycled in hybrid electrolyte also were tested. Figures 5a and 5b present the GCD curves and long-term cycling performance of the NNiHCF//AC full cell at 2 C (based on cathode active mass). The specific capacity of the initial cycle is approximately 50.2 mAh g^{-1}, with an average working voltage of 1.0 V. The capacity fades mostly at initial 500 cycles and the capacity retention of subsequent 4500 is only 80.5%. The overall discharge capacity retention is about 60.0% during 5000 cycles which is higher than that of NNiHCF in pure $(NH_4)_2SO_4$ electrolyte. To compare the electrochemical performance of the full rocking-chair AIBs presented in this work with similar systems reported in the previous literature, some of the most relevant performance metrics are summarized in Table S3.

The experimental results presented in Figures 5c and 5d illustrate the discharge capacity of the NNiHCF//AC full cell at various C-rates. The discharge capacity decreases with increasing rates due to the reaction rate limitations within the battery. At 2 C, the discharge capacity is 50.2 mAh g^{-1}, followed by 40.4, 35.6, 31.6, and 27.7 mAh g^{-1} at 3, 4, 6 and 10 C, respectively. These results indicate that the battery exhibits excellent rate performance, maintaining relatively high discharge capacity at

high rates. This achievement can be attributed to the fast migration rate of NH_4^+ ions, which enables faster ion transport within the battery. It is important to note that the addition of Ni^{2+} as an additive does not alter the charge storage mechanisms of NNiHCF electrode but suppress Ni dissolution. Over all, these results demonstrate the promising rate and cycling performance of the aqueous NH_4^+ ion battery, endowing it with potential competitiveness in large-scale energy storage applications.

Conclusions

In brief, a one-step co-precipitation method directly for synthesizing ammonium-rich Prussian blue material is developed. This approach shortens the synthesis period and reduces cost. The particle size of the as-prepared NNiHCF ranges from 0.4 to 200 nm. Moreover, NNiHCF exhibits excellent electrochemical performances and structural stability. During the charge-discharge process, NH_4^+ ions are highly reversible in terms of insertion into or extraction from NNiHCF lattice which are confirmed by *ex-situ* XRD results. Specifically, the capacity
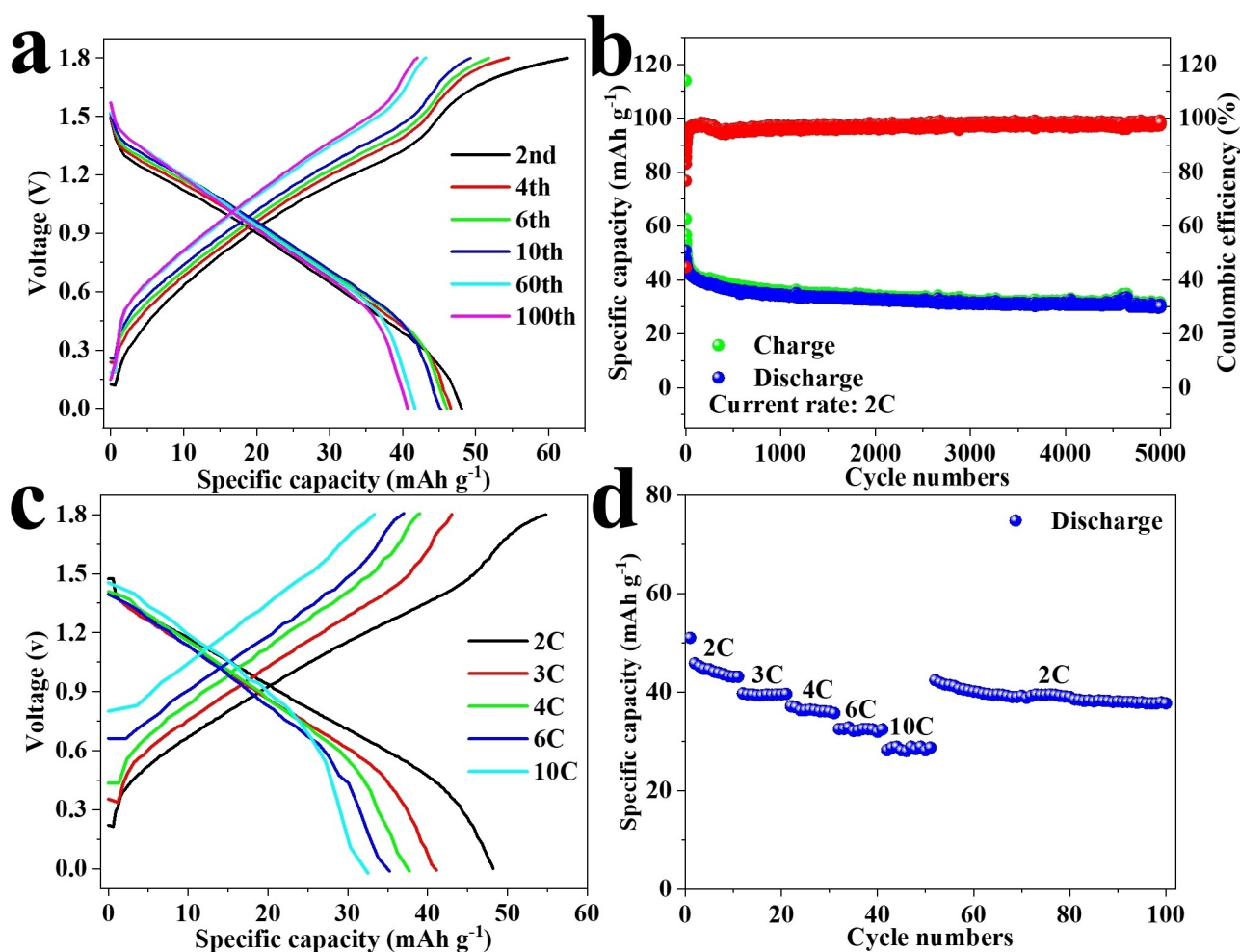
Figure 5. Electrochemical performances of aqueous NH4-ion full battery. a) Selected GCD curves from long cyclic performance at 2 C. b) Cycling performance at 2 C rate. c) and d). Rate performance, here 1 C ≈ 100 mA g^{-1}.

Batteries & Supercaps

Research Article
doi.org/10.1002/batt.202300546

Chemistry
Europe

European Chemical
Societies Publishing

retention reaches 60% after 5000 cycles at 2 C, indicating a long-term cycling stability of NNiHCF cathode. Therefore, there is hope for quick NH_4^+ storage with this stable cathode material with easy synthesis and long-term cycling capabilities.

Experimental Section

Material Preparation

NNiHCF was synthesized by a one-step aqueous precipitation method. Typically, 4 mmol of $NiSO_4 \cdot 6H_2O$ was dissolved in 40 mL of deionized (DI) water to form solution A. 4 mmol of $(NH_4)_2SO_4$ was dissolved in 40 mL of DI water to form solution B. Subsequently, the solution A and the solution B were added dropwise into 50 mL 0.1 mol L^{-1} $Na_4Fe(CN)_6 \cdot 10H_2O$ solution under stirring in turn. The resulting solution was then magnetically stirring at room temperature for 1 hours. The as-obtained precipitates were also rinsed with DI water for several times and dried in an oven at 60 °C. AC powder was a commercially available pigment and purchased from Sinopharm.

Material Characterization

XRD patterns of the samples were collected by a Bruker AXS D8Advance X-ray diffractometer using Cu–Kα radiation. XPS were collected by a Shimadzu/Kratos AXIS Ultra XPS spectrometer. All binding energies were referenced to the C 1s peak of 284.8 eV. The morphology and microstructure of the samples were examined by JSM-6390LV SEM. The chemical compositions of NNiHCF was determined by Agilent 720/725 inductively coupled plasma (ICP) on Ni and Fe elements, elemental analysis on C and N elements, and Netzsch STA 449 F3 thermogravimetric analysis (TGA) on crystal water. The concentration of dissolved Fe in the cycled electrolyte was tested using ICP. FTIR spectra were recorded using a 60-SXB IR spectrometer.

Electrochemical Measurements

The working electrodes of cathode (NNiHCF) and anode (AC) were prepared by the mixture of active materials, acetylene black and polyvinylidene fluoride (PVDF) in a mass of 8:1:1 in N-Methyl-2-pyrrolidone (NMP), producing a homogeneous slurry, and then cast on carbon paper current collector and dried at 60 °C in vacuum oven. The average active material mass loading was about 1 mg cm^{-2} for NNiHCF electrodes and 2.5 mg cm^{-2} for AC electrodes. The electrochemical performances of NNiHCF electrodes was examined in a typical three-electrode system, where NNiHCF electrode, graphite rod, and saturated calomel electrode (SCE, E = 0.244 V vs. standard hydrogen electrode, SHE) were employed as working electrode (WE), counter electrode (CE), and reference electrode (RE), respectively. The electrolyte for the NNiHCF electrode was homogeneous solution of 2.0 M $(NH_4)_2SO_4$ and 0.1 M $NiSO_4$. Aqueous full cells were fabricated in 2032 type coin cell, with

cathode to anode mass ratio of ~1:2.5. The as-prepared NNiHCF//AC were tested in a two-electrode system. The tests of electrochemical impedance spectroscopy (EIS) and cyclic voltammetry (CV) were performed on a CHI660E electrochemical workstation (Shanghai Chenhua Instrument Co., China). The GCD and long-term cyclic performances were recorded on a LAND battery test system (CT3001 A).

Conflict of Interests

The authors declare no conflict of interest.

Data Availability Statement

The data that support the findings of this study are available from the corresponding author upon reasonable request.

[1] a) X. Wang, J. Zhuang, Q. Peng, Y. Li, *Nature* **2005**, *437*, 121–124; b) Q. Liu, X. Su, D. Lei, Y. Qin, J. Wen, F. Guo, Y. A. Wu, Y. Rong, R. Kou, X. Xiao, F. Aguesse, J. Bareño, Y. Ren, W. Lu, Y. Li, *Nat. Energy* **2018**, *3*, 936–943; c) H. Zhang, G. G. Eshetu, X. Judez, C. Li, L. M. Rodriguez-Martínez, M. Armand, *Angew. Chem. Int. Ed.* **2018**, *57*, 15002–15027.

[2] a) Y. Zhang, H. Jiang, L. Xu, Z. Gao, C. Meng, *ACS Appl. Energ. Mater.* **2019**, *2*, 7861–7869; b) Z. Liu, H. Li, M. Zhu, Y. Huang, Z. Tang, Z. Pei, Z. Wang, Z. Shi, J. Liu, Y. Huang, C. Zhi, *Nano Energy* **2017**, *44*, 164–173; c) Y. Y. Liu, Z. H. Pan, D. Tian, T. Hu, H. M. Jiang, J. Yang, J. J. Sun, J. Q. Zheng, C. G. Meng, Y. F. Zhang, *Chem. Eng. J.* **2020**, *399*, 125842; d) T. T. Liu, X. Cheng, H. X. Yu, H. J. Zhu, N. Peng, R. T. Zheng, J. D. Zhang, M. Shui, Y. H. Cui, J. Shu, *Energy Storage Mater.* **2019**, *18*, 68–91; e) D. Kundu, E. Talaie, V. Duffort, L. F. Nazar, *Angew. Chem. Int. Ed.* **2015**, *54*, 3431–3448.

[3] a) S. Chen, R. Lan, J. Humphreys, S. Tao, *Energy Storage Mater.* **2020**, *28*, 205–215; b) E. Hosseini-Bab-Anari, A. Boschin, T. Mandai, H. Masu, K. Moth-Poulsen, P. Johansson, *RSC Adv.* **2016**, *6*, 85194–85201; c) R. A. Huggins, *J. Electrochem. Soc.* **2017**, *164*, A5031–A5036; d) A. Ramanujapuram, D. Gordon, A. Magasinski, B. Ward, N. Nitta, C. Huang, G. Yushin, *Energy Environ. Sci.* **2016**, *9*, 1841–1848; e) J. Shin, J. W. Choi, *Adv. Energy Mater.* **2020**, *10*, 2001386; f) S. Wang, L. Hu, X. Li, D. Qiu, S. Qiu, Q. Zhou, W. Deng, X. Lu, Z. Yang, M. Qiu, Y. Yu, J. Energy, *Chem.* **2024**, DOI: 10.1016/j.jechem.2023.12.005; g) J. Yang, W. Hou, L. Ye, G. Hou, C. Yan, Y. Zhang, *Small* **2024**, DOI: 10.1002/smll.202305386.

[4] a) Z. Hu, L. X. Wang, K. Zhang, J. B. Wang, F. Y. Cheng, Z. L. Tao, J. Chen, *Angew. Chem. Int. Ed.* **2014**, *53*, 12794–12798; b) H. Jiang, Y. Zhang, Y. Liu, J. Yang, L. Xu, P. Wang, Z. Gao, J. Zheng, C. Meng, Z. Pan, *J. Mater. Chem. A* **2020**, *8*, 15130–15139; c) T. T. Liu, X. K. Zhang, M. T. Xia, H. X. Yu, N. Peng, C. Jiang, M. Shui, Y. Xie, T. F. Yi, J. Shu, *Nano Energy* **2020**, *67*, 104295; d) H. X. Yu, X. Cheng, M. T. Xia, T. T. Liu, W. Q. Ye, R. T. Zheng, N. B. Long, M. Shui, J. Shu, *Energy Storage Mater.* **2019**, *22*, 154–159; e) Q. Zhang, J. Y. Luan, L. Fu, S. G. Wu, Y. G. Tang, X. B. Ji, H. Y. Wang, *Angew. Chem. Int. Ed.* **2019**, *58*, 15841–15847; f) T. N. T. Tran, M. Zhao, S. Geng, D. G. Ivey, *Batteries & Supercaps* **2022**, *5*, e202100420; g) S. Liu, W. Shang, Y. Yang, D. Kang, C. Li, B. Sun, L. Kang, S. Yun, F. Jiang, *Batteries & Supercaps* **2022**, *5*, e202100221.

[5] a) C. Y. Li, D. X. Zhang, F. X. Ma, T. Y. Ma, J. Wang, Y. H. Chen, Y. S. Zhu, L. J. Fu, Y. P. Wu, W. Huang, *ChemSusChem* **2019**, *12*, 3732–3736; b) Y. D. Zhang, Y. F. An, B. Yin, J. M. Jiang, S. Y. Dong, H. Dou, X. G. Zhang, *J. Mater. Chem. A* **2019**, *7*, 11314–11320; c) R. Zheng, Y. Li, H. Yu, X. Zhang, D. Yang, L. Yan, Y. Li, J. Shu, B. L. Su, *Angew. Chem. Int. Ed.* **2023**, *62*, e202301629.

[6] a) B. Q. Wang, Y. Han, X. Wang, N. Bahlawane, H. G. Pan, M. Yan, Y. Z. Jiang, *iScience* **2018**, *3*, 110–133; b) X. Y. Wu, Y. T. Qi, J. J. Hong, Z. F. Li, A. S. Hernandez, X. L. Ji, *Angew. Chem. Int. Ed.* **2017**, *56*, 13026–13030;

Batteries & Supercaps

Research Article
doi.org/10.1002/batt.202300546

Chemistry Europe
European Chemical
Societies Publishing

c) X. Zhang, M. Xia, H. Yu, J. Zhang, Z. Yang, L. Zhang, J. Shu, *Nano-Micro Lett.* **2021**, *13*, 139; d) W. Hou, C. Yan, P. Shao, K. Dai, J. Yang, *Nanoscale* **2022**, *14*, 8501–8509.

[7] M. R. Lukatskaya, O. Mashtalir, C. E. Ren, Y. Dall'Agnese, P. Rozier, P. L. Taberna, M. Naguib, P. Simon, M. W. Barsoum, Y. Gogotsi, *Science* **2013**, *341*, 1502–1505.

[8] a) H. Li, J. Yang, J. L. Cheng, T. He, B. Wang, *Nano Energy* **2020**, *68*, 104369; b) C. Xu, Z. Yang, X. Zhang, M. Xia, H. Yan, J. Li, H. Yu, L. Zhang, J. Shu, *Nano-Micro Lett.* **2021**, *13*, 166; c) X. Zhang, M. Xia, T. Liu, N. Peng, H. Yu, R. Zheng, L. Zhang, M. Shui, J. Shu, *Chem. Eng. J.* **2021**, *421*, 127767.

[9] Y. Song, Q. Pan, H. Z. Lv, D. Yang, Z. M. Qin, M. Y. Zhang, X. Q. Sun, X. X. Liu, *Angew. Chem. Int. Ed.* **2021**, *60*, 5718–5722.

[10] S. Y. Dong, W. Shin, H. Jiang, X. Y. Wu, Z. F. Li, J. Holoubek, W. F. Stickle, B. Key, C. Liu, J. Lu, P. A. Greaney, X. G. Zhang, X. L. Ji, *Chem* **2019**, *5*, 1537–1551.

[11] G. Liang, Y. Wang, Z. Huang, F. Mo, X. Li, Q. Yang, D. Wang, H. Li, S. Chen, C. Zhi, *Adv. Mater.* **2020**, *32*, 1907802.

[12] Q. Chen, M. D. Song, X. Y. Zhang, J. L. Zhang, G. Y. Hou, Y. P. Tang, *J. Mater. Chem. A* **2022**, *10*, 15614–15622.

[13] Z. Tian, V. S. Kale, Y. Wang, S. Kandambeth, J. Czaban-Jozwiak, O. Shekhah, M. Eddaoudi, H. N. Alshareef, *J. Am. Chem. Soc.* **2021**, *143*, 19178–19186.

[14] a) L. Jiang, Y. Lu, C. Zhao, L. Liu, J. Zhang, Q. Zhang, X. Shen, J. Zhao, X. Yu, H. Li, X. Huang, L. Chen, Y.-S. Hu, *Nat. Energy* **2019**, *4*, 495–503; b) L. Y. Zhang, L. Chen, X. F. Zhou, Z. P. Liu, *Adv. Energy Mater.* **2015**, *5*, 1400930.

[15] a) L. Chen, H. Z. Shao, X. F. Zhou, G. Q. Liu, J. Jiang, Z. P. Liu, *Nat. Commun.* **2016**, *7*, 11982; b) X. Wu, W. Deng, J. Qian, Y. Cao, X. Ai, H. Yang, *J. Mater. Chem. A* **2013**, *1*, 10130–10134.

[16] J. F. Qian, C. Wu, Y. L. Cao, Z. F. Ma, Y. H. Huang, X. P. Ai, H. X. Yang, *Adv. Energy Mater.* **2018**, *8*, 1702619.

[17] a) Y. You, X.-L. Wu, Y.-X. Yin, Y.-G. Guo, *J. Mater. Chem. A* **2013**, *1*, 14061–14065; b) X. K. Zhang, M. T. Xia, T. T. Liu, N. Peng, H. X. Yu, R. T. Zheng, L. Y. Zhang, M. Shui, J. Shu, *Chem. Eng. J.* **2021**, *421*, 127767.

[18] L. Chen, W. Sun, K. Xu, Q. Dong, L. Zheng, J. Wang, D. Lu, Y. Shen, J. Zhang, F. Fu, H. Kong, J. Qin, H. Chen, *ACS Energy Lett.* **2022**, *7*, 1672–1678.

[19] G. Du, M. Tao, J. Li, T. Yang, W. Gao, J. Deng, Y. Qi, S. J. Bao, M. Xu, *Adv. Energy Mater.* **2019**, *10*, 1903351.

[20] Y. Xu, M. Ou, Y. Liu, J. Xu, X. Sun, C. Fang, Q. Li, J. Han, Y. Huang, *Nano Energy* **2020**, *67*, 104250.

[21] C. D. Wessells, S. V. Peddada, R. A. Huggins, Y. Cui, *Nano Lett.* **2011**, *11*, 5421–5425.

[22] Q. Jiang, N. Kurra, M. Alhabeb, Y. Gogotsi, H. N. Alshareef, *Adv. Energy Mater.* **2018**, *8*, 1703043.

[23] Y. Q. Jiang, J. P. Liu, *Energy Environ. Mater.* **2019**, *2*, 30–37.

[24] a) C. Xia, J. Guo, Y. Lei, H. Liang, C. Zhao, H. N. Alshareef, *Adv. Mater.* **2017**, *32*, 1907798; b) J. Wang, J. Polleux, J. Lim, B. Dunn, *J. Phys. Chem. C* **2007**, *111*, 14925–14931.

[25] X. Y. Wu, Y. K. Xu, H. Jiang, Z. X. Wei, J. J. Hong, A. S. Hernandez, F. Du, X. L. Ji, *ACS Appl. Energ. Mater.* **2018**, *1*, 3077–3083.

[26] H. Li, X. Q. Yu, Y. Bai, F. Wu, C. Wu, L. Y. Liu, X. Q. Yang, *J. Mater. Chem. A* **2015**, *3*, 9578–9586.

[27] C. D. Wessells, R. A. Huggins, Y. Cui, *Nat. Commun.* **2011**, *2*, 550.

[28] X. Zhang, M. Xia, H. Yu, J. Zhang, Z. Yang, L. Zhang, J. Shu, *Nano-Micro Lett.* **2021**, DOI: 10.1007/s40820-021-00671-x.

[29] W. Hou, C. Yan, P. Shao, K. Dai, J. Yang, *Nanoscale* **2022**, *14*, 8501–8509.

[30] J. Han, M. Zarrabeitia, A. Mariani, M. Kuenzel, A. Mullaliu, A. Varzi, S. Passerini, *Adv. Mater.* **2022**, DOI: 10.1002/adma.202201877.

[31] S. Krishnan, D. K. Rai, X. Wang, *ACS Appl. Polym. Mater.* **2023**, DOI: 10.1021/acsapm.3c01739.